Lawrence Berkeley National Laboratory
LBL Publications

Title
Programable Beam Control for Electron Energy-Loss Spectroscopy and Ptychography

Permalink
https://escholarship.org/uc/item/5k3739rd

Journal
Microscopy and Microanalysis, 32(4)

ISSN
1431-9276

Authors
Palos, Mariana
Spillane, Liam
Topore, Geri
et al.

Publication Date
2026-07-01

DOI
10.1093/mam/ozag080

Copyright Information
This work is made available under the terms of a Creative Commons Attribution License, available at https://creativecommons.org/licenses/by/4.0/

Peer reviewed

eScholarship.org Powered by the California Digital Library
University of California

Programable Beam Control for Electron Energy-Loss Spectroscopy and Ptychography

Mariana Palos, Liam Spillane, Geri Topore, Yaqi Li, David Pesquera, Colin Ophus, Stephanie M Ribet, Michele Shelly Conroy

Downloaded from academic.oup.com/mam/article/32/4/ozag080/8754136 by guest on 10 November 2026

DECTRIS QUADRO

The flexible standard for **electron microscopy**
Maximizing performance on a single platform



Microscopy and Microanalysis, 2026, **32**, ozag080
https://doi.org/10.1093/mam/ozag080
Advance access publication 7 August 2026
Original Article

Microscopy AND Microanalysis

Programable Beam Control for Electron Energy-Loss Spectroscopy and Ptychography

Mariana Palos[1], Liam Spillane[2], Geri Topore[1], Yaqi Li[1], David Pesquera[3], Colin Ophus[4], Stephanie M. Ribet[5], and Michele Shelly Conroy[1,*]

[1]*Department of Materials, London Centre of Nanotechnology, Imperial College London, Exhibition Road, London SW7 2AZ, UK*
[2]*Gatan Inc., 5794 W. Las Positas Blvd., Pleasanton, CA 94588, USA*
[3]*Catalan Institute of Nanoscience and Nanotechnology (ICN2), Bellaterra, Barcelona 08193, Spain*
[4]*Department of Materials Science and Engineering, Stanford University, Stanford, CA 94305, USA*
[5]*National Center for Electron Microscopy, Molecular Foundry, Lawrence Berkeley National Laboratory, Berkeley, CA 94720, USA*

***Corresponding author:** Michele Shelly Conroy, E-mail: mconroy@imperial.ac.uk

Abstract

Programable electron-beam scanning offers new opportunities to improve dose efficiency and suppress scan-induced artifacts in scanning transmission electron microscopy. Here, we systematically benchmark the impact of non-raster trajectories, including spiral and multi-pass sequential patterns, on electron energy-loss spectroscopy (EELS) and ptychography. Using $DyScO_3$ as a model perovskite, we compare spatial resolution, spectral fidelity, and artifact suppression across scan modes. Ptychographic phase reconstructions consistently achieve atomic resolution and remain robust to large jumps in probe position. In contrast, atomic-resolution EELS maps show pronounced sensitivity to probe motion, with sequential and spiral scans introducing non-uniform elemental contrast. Finally, spiral scanning applied under cryogenic conditions in BTO thin films improves dose uniformity and mitigates drift-related distortions. These results establish practical guidelines for the implementation of non-raster scan strategies in 4D-STEM and highlight the inherent resilience of ptychography to trajectory-induced artifacts.

Key words: 4D-STEM, cryogenic microscopy dose efficiency radiation damage, electron energy-loss spectroscopy (EELS), programable beam scanning, ptychography, scanning transmission electron microscopy (STEM)

Introduction

Scanning transmission electron microscopy (STEM) techniques are inherently sensitive to dose distribution, as image and spectral quality depend not only on the total accumulated dose but also on how that dose is delivered in space and time during scanning. In this work, we focus on real-space STEM imaging, electron energy-loss spectroscopy (EELS), and four-dimensional STEM (4D-STEM). EELS provides insight into electronic structure, bonding, and low-energy excitations such as phonons. Advances in aberration-corrected STEM, detector and spectrometer technology, improved monochromators, and quantitative analysis methods have expanded the capabilities of EELS to include atomic-resolution chemical mapping and energy resolutions ranging from the sub-eV regime for core-loss spectroscopy to the meV scale for vibrational and low-loss studies (Egerton, 2003; Verbeeck & Van Aert, 2004; Egoavil et al., 2014).

4D-STEM records a diffraction pattern at each probe position as shown in Figure 1a, providing access to position-sensitive structural information, which can be used to map ordering in materials at high-resolutions including probing strain and electromagnetic field information. 4D-STEM-based phase retrieval methods, such as iterative electron ptychography, allow for high-resolution, dose-efficient characterization of structure through reconstruction of real space potential (Ophus, 2019; Savitzky et al., 2021; Ophus, 2023; Varnavides et al., 2024).

Ptychography is an iterative phase-retrieval technique in which overlapping probe positions illuminate each region of a specimen multiple times from slightly different probe positions, enabling simultaneous reconstruction of both the object transmission function and the probe wavefront. A deliberately defocused probe can be rastered across the specimen with a less dense scan pattern, lowering the instantaneous dose at each probe position, while increasing probe overlap compared to focused ptychography. Defocusing has the advantage of larger and adjustable probe size, which can reduce the impact of positional instabilities, arising from various sources on the ptychographic reconstruction (Mille et al., 2022).

Both EELS and 4D-STEM demand relatively high electron doses, making beam-induced damage a critical limitation, particularly for organic, hybrid, and oxide materials where radiolysis dominates (Velazco et al., 2022). While low-dose workflows combining EELS and 4D-STEM are feasible, the spatial and temporal distribution of the dose can be as important as the total dose itself. Jannis et al. demonstrated that interleaved, spiral, and random scan trajectories can delay the onset of damage, reducing structural degradation in zeolites by up to 11% under equivalent total dose conditions (Velazco et al., 2020; Jannis et al., 2022*b*). These findings underscore that controlling how, not just how much, dose is delivered can preserve structure and chemistry in beam-sensitive systems.

Received: September 23, 2025. **Revised:** July 13, 2026. **Accepted:** July 13, 2026
© The Author(s) 2026. Published by Oxford University Press on behalf of the Microscopy Society of America.
This is an Open Access article distributed under the terms of the Creative Commons Attribution License (https://creativecommons.org/licenses/by/4.0/), which permits unrestricted reuse, distribution, and reproduction in any medium, provided the original work is properly cited.

Downloaded from academic.oup.com/mam/article/32/4/ozag080/8754136 by guest on 10 November 2026

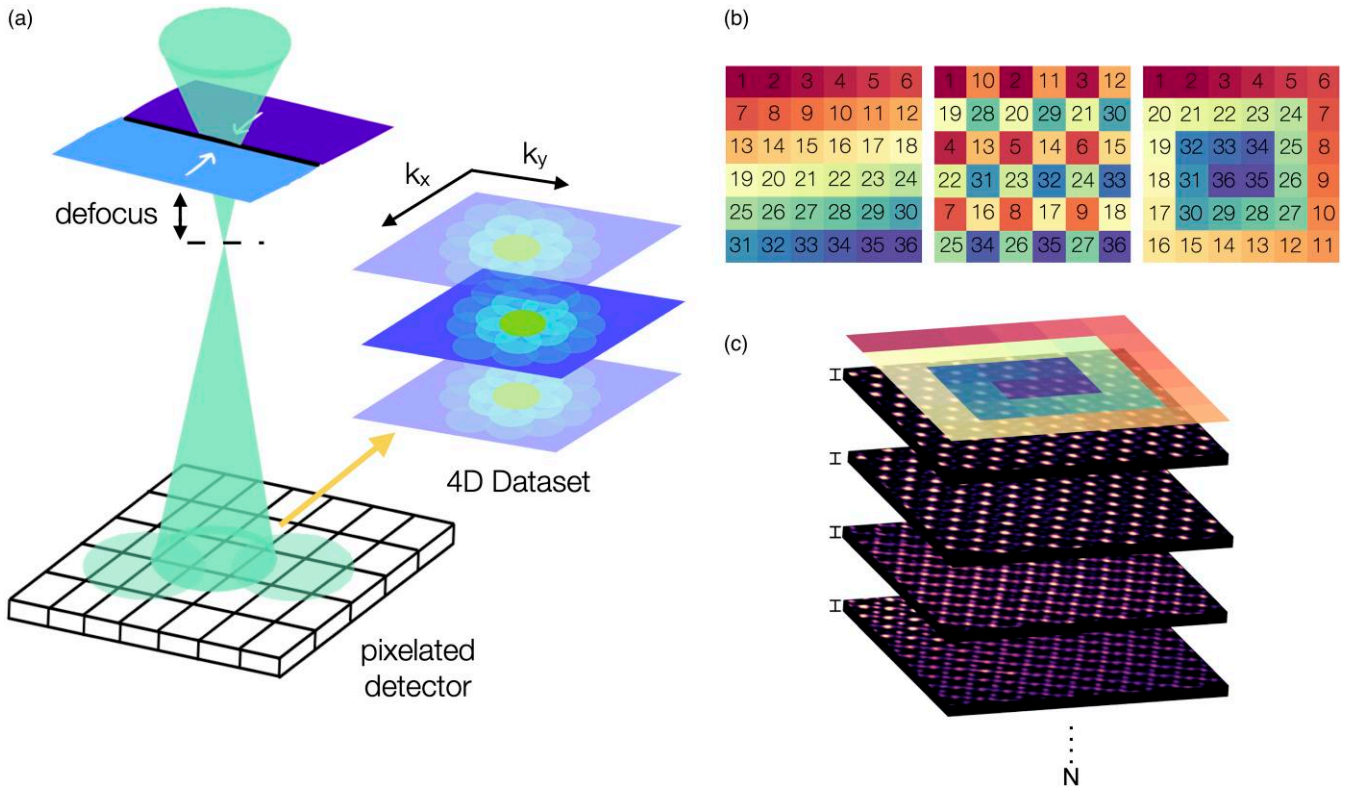


Fig. 1. (**a**) Schematic of the 4D-STEM experimental setup used in this study. A defocused electron probe is scanned across the sample, while 2D diffraction patterns are recorded at each probe position using a pixelated detector (Gatan K3) (**b**) Examples of programable scan trajectories include raster, 2 × 2 N-sequential, and spiral (inward) patterns. (**c**) Illustration of a multislice ptychography reconstruction, with a spiral scan path overlaid on the first slice, demonstrating compatibility between custom scan strategies and ptychographic phase retrieval.

Cryogenic STEM provides a route for imaging fragile materials and stabilizing low-temperature phases without inducing structural changes. However, cryogenic workflows introduce additional challenges: increased drift, reduced signal-to-noise ratio (SNR), and higher contamination risk. Under these conditions, precise alignment, active drift correction, and dose-efficient acquisition strategies become essential. Programable scan paths, such as spiral and sparse, can mitigate these challenges by reducing localized hot spots and eliminating dwell time accumulation along raster flyback lines (Savitzky et al., 2018; Goodge et al., 2021; Pei et al., 2023).

The trajectory of the electron probe in STEM has a strong influence on the fidelity of both structural and spectroscopic data. Conventional raster scanning is prone to flyback delays, probe lag, and drift-induced distortions. To overcome these limitations, programable scan patterns, such as spiral, pixel-skipping, sparse, random, and interleaved paths, have been developed to improve dose uniformity, reduce motion-induced distortion, minimize damage, and eliminate flyback artifacts (Sang et al., 2016, 2017; Ede & Beanland, 2020; Nicholls et al., 2020; Zobelli et al., 2020; Ortega et al., 2021; Velazco et al., 2022). Implementing such trajectories requires precise synchronization of scan control, beam blankers, and high-speed detectors. Recent advances, including electromagnetic beam blankers (Béché et al., 2016), adaptive scanning (Turner et al., 2020; Mullarkey et al., 2022), flyback compensation algorithms (Peters et al., 2024), and event-driven acquisition with Timepix3 detectors (Jannis et al., 2022*a*) have made real-time and dose-efficient scanning increasingly practical.

In this work, we evaluate how different programable scan patterns affect spatial and spectral fidelity, with a focus on ptychographic phase retrieval (Fig. 1c) and EELS. Figure 2 shows the pixel acquisition order for the scanning patterns employed in this work. In the N-sequential approach (Figs. 2d, 2e), the probe samples every *N*th pixel during each pass before returning to fill the remaining positions, such that increasing *N* increases the instantaneous jump distance between successive probe positions while preserving the same nominal pixel grid after all passes. As highlighted by Nicholls et al. (2020), the optimal inter-pixel spacing depends on the physical properties of the material, including diffusivity, beam sensitivity, and lattice response. A random scan (Fig. 2f) is implemented by assigning a random permutation to the list of pixel coordinates and scanning in that order. Finally, a rectangular spiral trajectory is implemented in two directions: an inward spiral beginning at the top-left corner and continuously progressing toward the center of the region of interest (Fig. 2b), and an outward spiral beginning at the center and moving toward the edges.

Our motivation for testing these scans, was to systematically vary inter-pixel spacing and dose distribution, which are known to influence motion sensitivity, beam-induced diffusion, and spectroscopic stability in beam-sensitive oxides. Using $DyScO_3$ at room temperature, we benchmark these strategies for spatial resolution and artifact suppression. We then applied spiral scanning to free-standing cryogenic $BaTiO_3$ thin films to assess their ability to resolve light elements while minimizing beam-induced damage. These results provide practical guidelines for optimizing scan trajectories in high-resolution STEM workflows.

Downloaded from academic.oup.com/mam/article/32/4/ozag080/8754136 by guest on 10 November 2026

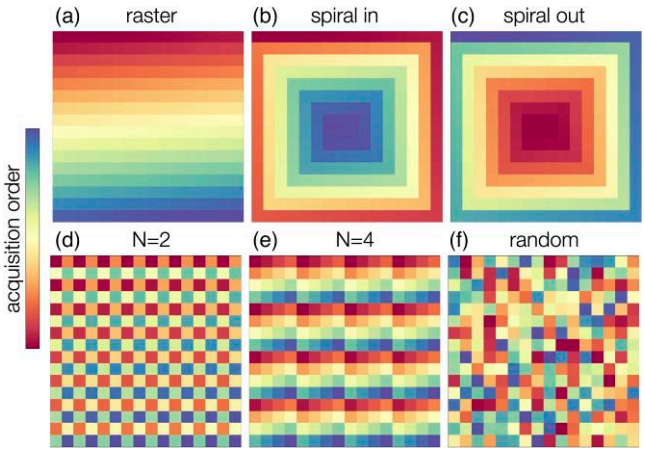


Fig. 2. Schematic of scan path variations: (**a**) raster, (**b**) inward spiral, (**c**) outward spiral, (**d**) 2 × 2 sequential, (**e**) 4 × 4 sequential, and (**f**) random. The color scale indicates the acquisition order, progressing from red (first pixels acquired) to blue (last pixels acquired).

Beyond imaging, tailored beam trajectories can play an important role in studies that explore how beam-specimen interactions actively modify materials, such as enabling manipulation of dopants and defects in 2D materials (Lin et al., 2014; Susi et al., 2017; Dyck et al., 2019) and control of domain wall motion in ferroelectrics (Hart et al., 2016; Chezganov et al., 2019; Barzilay & Ivry, 2020; Conroy et al., 2020; Volk et al., 2020; Roede et al., 2021). Understanding how scan patterns influence both measurement quality and material response is therefore critical for designing robust experiments.

Materials and Methods

Samples

Two perovskite oxide systems were examined in this study. $DyScO_3$ (DSO) was used as a structurally robust reference material for benchmarking programable scan performance at atomic resolution. A free-standing $BaTiO_3$ (BTO) membrane was used to evaluate cryogenic 4D-STEM for resolving light elements in a mechanically unsupported thin film.

$DyScO_3$

DSO was prepared from a commercial single-crystal substrate (orthorhombic *Pbnm* structure) oriented along the [001] zone axis, which provides the characteristic dumbbell-shaped cation columns. Cross-sectional TEM lamellae were prepared using a focused ion beam (FIB) lift-out procedure. The final specimen thickness was estimated to be 20–30 nm.

Free-standing BTO membranes

The BTO sample investigated under cryogenic conditions was an epitaxial thin film grown by pulsed laser deposition (PLD) on a water-soluble sacrificial layer of $Sr_3Al_2O_6$ (SAO). The direction of the growth and thus the imaging direction is [001] tetragonal zone axis. Following growth, the film was released by dissolving the SAO layer in deionized water and subsequently transferred onto a silicon nitride TEM window, resulting in a mechanically unsupported (free-standing) membrane. The membrane thickness, estimated from multislice ptychographic reconstructions, was approximately 5–10 nm.

Instrumentation

All measurements were performed on a Thermo Fisher Spectra 300 S/TEM operating at 300 kV, equipped with a Gatan K3 direct electron detector positioned beneath a differential phase contrast(DPC) quadrant detector.

For low temperature experiments, the BTO samples were cooled to ~100 K using a Gatan Elsa cryo holder.

Scan Control and Software

All programable scan trajectories used in this work were executed using Gatan DigitalMicrograph (GMS 3.62) together with the DigiScan 3 scan engine. Raster, inward/outward spiral, random, and N-sequential scan modes (Fig. 2) are implemented natively in the DigiScan interface, and therefore no custom scripts are required to reproduce these trajectories. Users may freely download GMS 3.62; however, access to programable scan modes requires compatible DigiScan 3 hardware. The DigiScan line flyback time is set to ≈200 μs for conventional raster acquisition. In arbitrary and N-sequential scan modes, no line-by-line flyback is applied; instead, the scan engine executes point-to-point coordinate updates directly from the scan list.

EELS Data Acquisition

STEM–EELS spectrum imaging was performed using a Gatan GIF spectrometer. A 5 mm GIF entrance aperture was used, corresponding to a nominal collection semi-angle of approximately 160 mrad.

Each EELS map consisted of a 128 × 128 grid with a step size of 0.04 nm (0.4 Å), producing a field of view of 5.1 nm. A pixel dwell time of 0.677 ms was used. Fifteen passes were collected with drift correction between passes. The total acquisition time per map was ~4 min 27 s.

Dual-EELS mode was used with a dispersion of 0.9 eV/channel. The low-loss signal (acquired at reduced live time) was used solely for energy-axis alignment of the high-loss spectra. The probe current during EELS acquisitions was ~40 pA.

For each EELS acquisition, an ADF signal was recorded in parallel. ADF-STEM images shown alongside EELS maps correspond to the sum ADF frames recorded during the 15-pass EELS acquisition. Drift correction was applied between passes. These ADF images were used to assess scan-pattern–dependent artifacts.

EELS Processing and Artifact Quantification

EELS spectra and maps of the Dy *M*, Sc *L*, and O *K* edges were first energy-aligned using the zero-loss peak. Background subtraction, denoising, and mild Savitzky-Golay smoothing were applied consistently to all datasets. Elemental maps were quantified as areal density maps using PCA denoising with three components. Identical processing parameters were used for all scan patterns to ensure that differences observed between datasets arise from scan trajectory effects rather than post-processing.

To visualize scan-induced distortions in reciprocal space, Fast Fourier Transforms (FFTs) of both ADF images and Dy EELS maps were computed after application of a Hanning window to suppress edge effects. The FFT magnitude was log-scaled, percentile-filtered, and centrally cropped to

Downloaded from academic.oup.com/mam/article/32/4/ozag080/8754136 by guest on 10 November 2026

enhance visibility of lattice reflections and trajectory-specific artifacts.

The positions of the atomic columns were extracted from the raster ADF reference image and from the Dy EELS maps obtained with each scan trajectory using Atomap (Nord et al., 2017). Initial peak positions were identified using feature separation analysis, followed by center-of-mass refinement and 2D Gaussian fitting to determine sub-pixel atomic column coordinates. Zone axes were constructed from the refined lattice to identify atomic planes and measure inter-column distances. From these refined coordinates, nearest-neighbor distances, positional deviations relative to the ADF reference, and lattice angles were quantified. This analysis follows the approach used by Torruella et al. (2025) for evaluating the fidelity of atomic column positions in EDX elemental maps, where Atomap-based refinement is used to assess positional accuracy, column definition, and map quality. This methodology provides an objective metric to compare how different scan trajectories affect the spatial fidelity of EELS elemental maps relative to the ADF.

4D-STEM Data Acquisition

The probe current during 4D-STEM acquisitions was maintained at ~5 pA for all scans.

The scan areas typically consisted of 64×64 probe positions, with diffraction patterns recorded at each point. The probe step size was 0.7 Å, corresponding to a field of view of approximately 4.5 nm. A pixel dwell time of 3.3 ms was used for most acquisitions. The defocus was varied between 10 and 20 nm, optimized manually for each dataset. Variations in sample thickness and defocus were minimized, but not eliminated, across the different scan pattern datasets.

For a representative ptychographic dataset (64×64 scan, 0.7 Å step size, 3.3 ms dwell, 5 pA probe current), the electron dose was approximately 2.1×10^5 $e^-/Å^2$. This corresponds to $\sim 1.0 \times 10^5$ electrons per probe position and a total of $\sim 4.2 \times 10^8$ electrons distributed over a 4.5 nm field of view.

Ptychographic Reconstructions

Ptychographic reconstructions were performed using the `py4DSTEM` software package, employing a multi-slice mixed-state algorithm with 10–20 slices (2 nm per slice) (Savitzky et al., 2021; Varnavides et al., 2024). For the DSO, two probe modes were used, while for the cryogenic BTO reconstructions six probe modes were required to accurately describe the experimental probe. All reconstructions were performed with consistent settings to facilitate comparison. Reconstructions were evaluated using phase image analysis FFTs to assess the highest resolvable Bragg peaks.

Experimental Results

The orthorhombic *Pbnm* lattice of DyScO3 ($a_o \neq b_o$) can be described in a pseudocubic framework following the standard transformation (Mundet et al., 2024). In this representation, the in-plane lattice parameters are equal in magnitude and given by

$$a_{pc} = b_{pc} = \frac{\sqrt{a_o^2 + b_o^2}}{2} \approx 3.95 \text{ Å}$$

while the orthorhombic distortion manifests as a deviation from 90° in the angle between the pseudocubic axes. For the [001] projection, this results in an expected in-plane angle of approximately 87°.

To verify that the apparent shear in our HAADF-STEM images originates from this crystallographic geometry rather than from scan-induced distortion, we extracted atomic column positions from the raster HAADF reference dataset using Atomap. Analysis of the refined zone vectors yielded angles of $88.8° \pm 0.04°$ and $1.6° \pm 0.04°$ relative to the horizontal axis, corresponding to an inter-axis angle of $87.2° \pm 0.06°$. This agrees with the expected *Pbnm* pseudocubic projection. Therefore, the lattice shear observed in DSO images reflects the intrinsic structure of the single-crystal substrate and is not an artifact introduced by the programable scan trajectories.

Atomic-Resolution EELS Mapping in DSO

DSO was selected as a model perovskite oxide to benchmark programable scan performance because of its well-defined orthorhombic crystal structure, resolvable oxygen columns for quantitative mapping, and stability under electron irradiation. Atomic-resolution Sc *L*-edge and Dy *M*-edge EELS maps were acquired using raster, spiral, random, and *N*-sequential scan patterns (Fig. 3). All scan trajectories produced interpretable elemental contrast, but differences in atomic-column continuity, positional definition, and intensity uniformity were evident. In several cases, discontinuities between neighboring columns visibly followed the underlying probe path. Additional elemental maps, including oxygen, are provided in Supplementary Figure S1, while quantitative line-profile comparisons of the Dy *M*-edge intensity across scan trajectories are presented in Supplementary Figure S2, highlighting the reduced peak definition and intensity suppression observed for the random and $N = 4$ sequential scans relative to raster, spiral, and $N = 2$ trajectories.

To characterize these differences, FFTs were computed from both the simultaneously acquired ADF images (Fig. 3 (row 3)) and the Dy elemental maps (Fig. 3 (last row)).

For raster and spiral scans, the FFTs show well-defined Bragg reflections consistent with the DSO *Pbnm* [001] projection. In the Dy FFT of the raster scan, orthorhombic half-order reflections arising from octahedral tilts are clearly visible, indicating preservation of crystallographic information at intermediate spatial frequencies.

In contrast, the *N*-sequential scans introduce additional peaks that do not correspond to DSO reflections. These are most pronounced for $N = 4$ in the ADF FFT (white circles in Fig. 3) and remain weakly visible in the Dy FFT (red arrows). As the inter-pixel jump distance increases (0.8 Åfor $N = 2$, 1.6 Åfor $N = 4$), these features become stronger and extend to spatial frequencies beyond the resolvable lattice information.

Notably, these jump distances represent significant fractions of the projected DSO nearest-neighbour column spacing (~3.7 Å). For $N = 2$, the probe repeatedly revisits columns with an offset of ~22% of the lattice spacing, while for $N = 4$ this offset increases to ~43%. As the imposed sampling periodicity approaches the intrinsic lattice periodicity, the scan trajectory increasingly interferes with the crystallographic signal. This explains why the additional FFT peaks and loss of column definition are weak for $N = 2$ but become pronounced for $N = 4$.

A further indication of scan-induced degradation is the systematic suppression of orthorhombic half-order reflections in the Dy FFTs (blue arrows in Fig. 3):

Downloaded from academic.oup.com/mam/article/32/4/ozag080/8754136 by guest on 10 November 2026

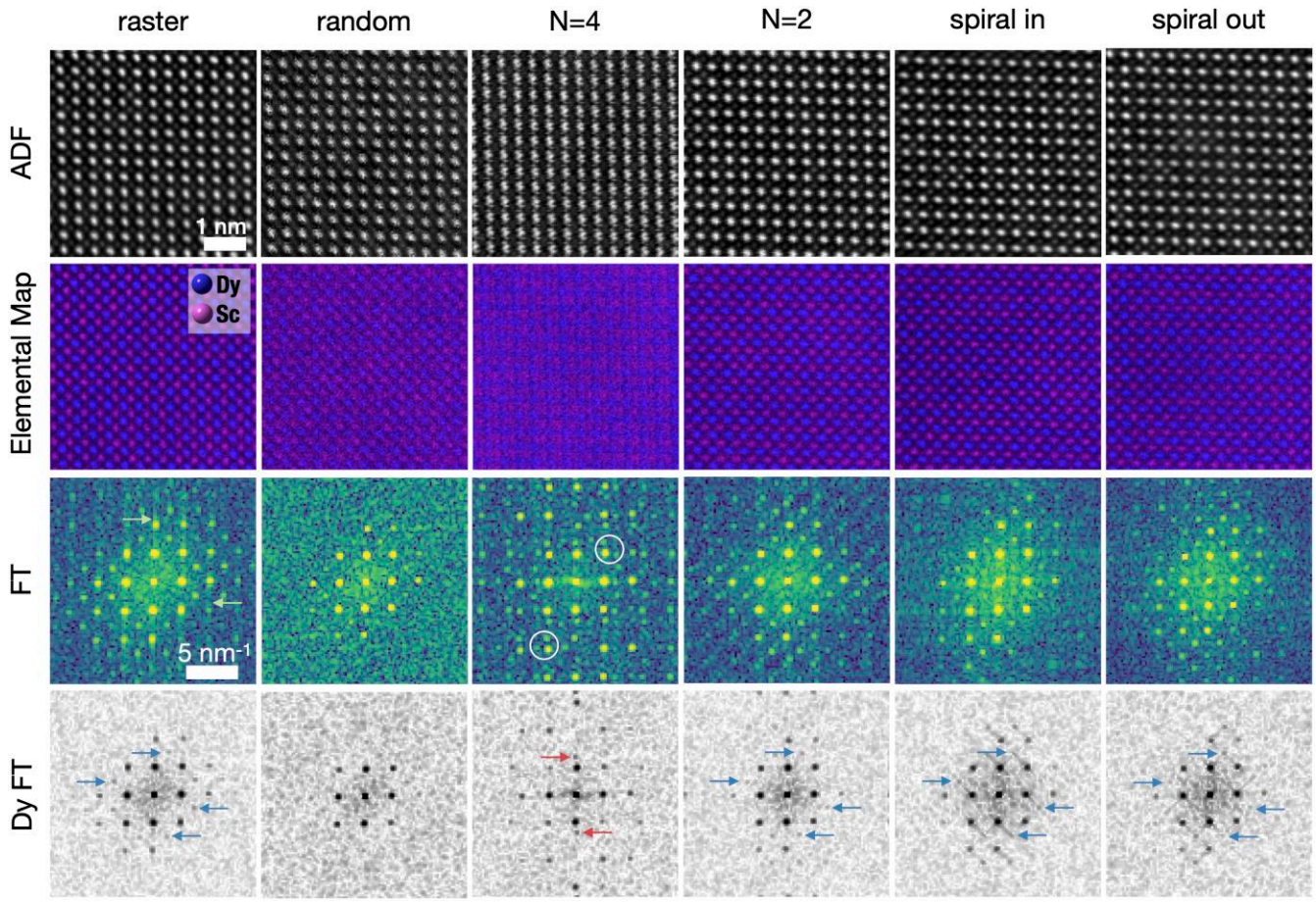


Fig. 3. ADF-STEM and EELS characterization of DSO acquired with different scan trajectories: raster, random, $N = 4$, $N = 2$ sequential, spiral-in, and spiral-out (columns from left to right). The first row shows ADF-STEM images for each scan, highlighting variations in contrast and signal continuity. The second row presents corresponding EELS elemental maps, with Dy in blue and Sc in pink. The third row shows Fourier transforms (FTs) of the ADF images; in the raster FTs, green arrows indicate directional streaking from flyback motion, while in the $N = 4$ FTs, white circles mark satellite peaks arising from large probe jumps. The fourth row shows FTs of the Dy EELS maps, where blue arrows indicate half-order reflections from the orthorhombic superlattice. These reflections are visible in raster scans, spiral-in/out scans, and faintly in $N = 2$, but are absent in $N = 4$ and random scans; red arrows highlight satellite peaks in $N = 4$.

Scan pattern	Half-order reflections in Dy FFT
Raster	clearly visible
$N = 2$	clearly visible
Spiral in and out	reduced
$N = 4$	absent
Random	absent

Because these reflections arise from subtle octahedral tilts, their disappearance indicates loss of crystallographic information in the elemental maps rather than a simple change in visual contrast.

Compared with spiral scans, raster FFTs show faint vertical streaking characteristic of line-to-line distortions during sequential acquisition. The spiral FFT exhibits sharper Bragg peaks and higher spatial-frequency extent than the random or $N = 4$ scans, although slight anisotropy remains. Random scans lack periodicity, producing weaker and less coherent FFT features.

Together, these observations demonstrate that scan trajectory influences not only real-space appearance but also the preservation of crystallographic information in elemental maps.

Quantitative Atomic Position Analysis

To quantify positional fidelity, atomic column positions were extracted from the Dy maps using Atomap and compared to the raster ADF reference (Fig. 4). The Dy mean nearest-neighbour spacing measured in the ADF reference was 3.69 Å, in agreement with the expected projected DSO spacing.

Figure 4h summarizes the mean spacings and standard deviations obtained for each scan trajectory. The conventional raster EELS map yields a spacing of 3.66 Å(−0.8% relative to HAADF), indicating good positional agreement. Spiral trajectories produce slightly larger spacings, with spiral out measuring 3.73 Å(+1.0%) and spiral in 3.75 Å(+1.5%). The $N = 2$ sequential scan shows a similar trend (3.76 Å, +1.9%). In contrast, scan strategies involving larger probe jumps show systematic underestimation: the random scan yields 3.59 Å(−2.7%), while the $N = 4$ sequential scan shows the largest deviation at 3.53 Å(−4.3%).

The spread in measured positions follows the same trend. Raster and spiral scans maintain relatively small standard deviations (~0.04–0.07 Å), consistent with continuous atomic columns in the elemental maps. In contrast, the random and N=4 scans exhibit much larger scatter (0.17 Åand 0.23 Å,

Downloaded from academic.oup.com/mam/article/32/4/ozag080/8754136 by guest on 10 November 2026

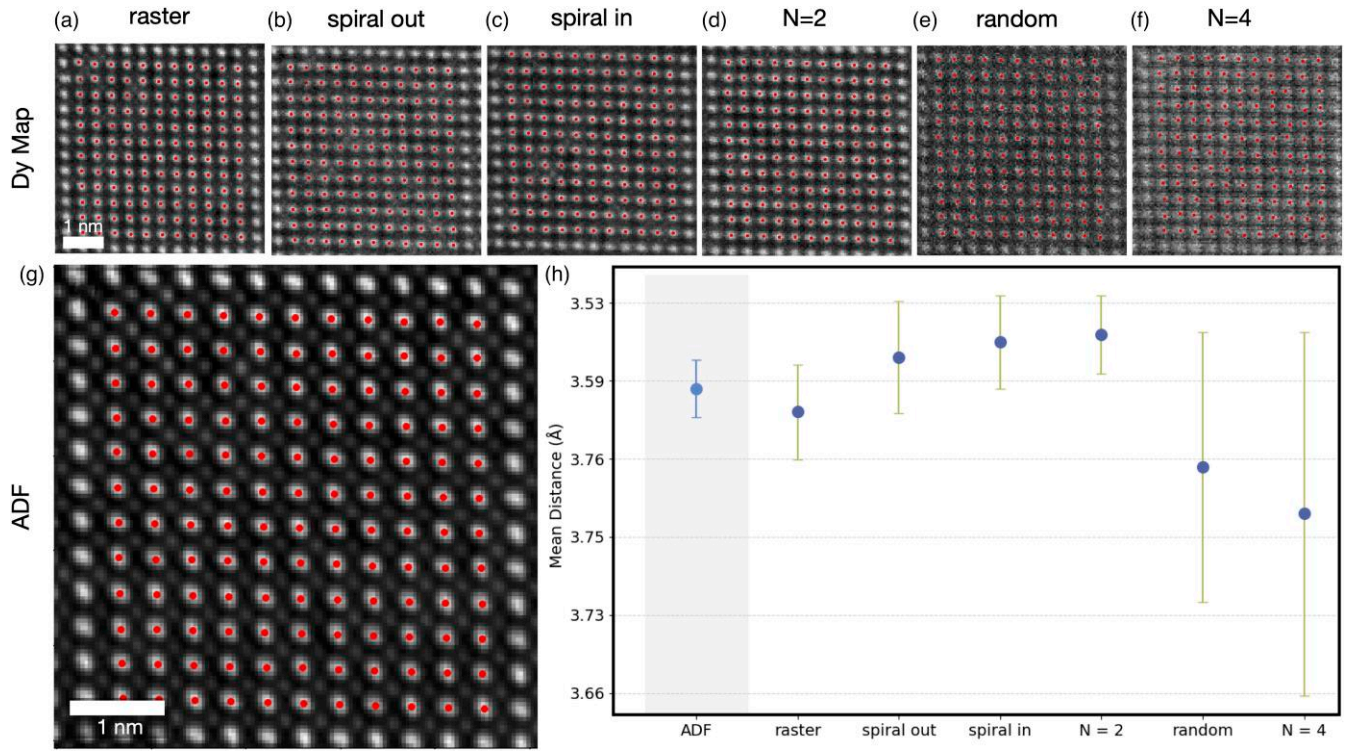


Fig. 4. Dy EELS atomic maps of $DyScO_3$ ordered from closest to the expected crystallographic mean to farthest as follows: (**a**) raster, (**b**) spiral out, (**c**) spiral in, (**d**) $N = 2$, (**e**) random, and (**f**) $N = 4$. Overlaid on each map are the atomic positions identified and refined using Atomap. Panel (**g**) shows the corresponding ADF raster image with the same Atomap refinement, which was used as the reference for nearest-neighbour distance measurements. (**h**) shows the mean nearest-neighbour distance measured for the ADF reference (3.69 Å) and for all scan patterns, with corresponding standard deviations.

respectively), reflecting the atomic discontinuities and local distortions visible in the corresponding Dy maps.

Overall, scan trajectories that introduce large instantaneous probe displacements degrade positional precision and increase variability in the recovered atomic coordinates. Even when the underlying lattice periodicity remains detectable, these distortions bias interatomic spacing measurements and reduce confidence in quantitative atomic-position analysis.

Ptychographic Reconstructions in $DyScO_3$

In contrast to the scan-dependent variations observed in ADF and EELS maps, the ptychographic phase reconstructions from DSO shown in Figure 5 revealed minimal differences in achievable resolution across N-sequential scan patterns. To further probe the limits of scan-induced effects on ptychography, an additional $N = 8$ trajectory was included, introducing probe jumps approaching the projected lattice spacing. Reconstructions obtained from all N-sequential scans ($N = 2, 4, 8$) exhibit clear atomic columns and well-defined lattice contrast.

FFTs of the reconstructed phase images shown in Figure 5 reveal Bragg reflections extending to ~0.7 Å for all N-sequential scans, including $N = 8$, where probe jumps approach the projected interatomic spacing. The visibility and sharpness of these reflections remain comparable across scan patterns, with no evidence of probe-position or trajectory-related artifacts that were prominent in the corresponding ADF and EELS datasets.

Unlike direct imaging modes, where positional errors translate directly into real-space distortions, ptychography relies on redundant, overlapping diffraction measurements and iterative phase retrieval. As long as sufficient probe overlap and reciprocal-space sampling are maintained, the reconstruction tolerates substantial scan-path irregularities and recovers high-resolution phase information even from non-ideal trajectories. Under the present acquisition conditions (defocused probe reconstructed with two probe modes), no improvement in lateral resolution is observed between scan patterns, and features such as Dy dumbbell splitting remain unresolved. These results demonstrate that, within this regime, ptychographic image quality is largely decoupled from probe trajectory, in contrast to ADF and EELS imaging. Representative mixed-state probe modes used in the multislice reconstructions are shown in Supplementary Figure S3, illustrating the two probe states used to model the experimental electron probe for the DSO datasets.

Cryogenic Spiral Scanning in Free-Standing BTO

To evaluate programable scanning under beam-sensitive conditions, we next applied spiral scanning to free-standing BTO thin films, imaged at cryogenic temperatures. Outward spiral scans produced ptychographic reconstructions that clearly resolved oxygen columns (Fig. 6c), with minimal drift or distortion despite the increased mechanical and electrostatic instability typical of cryo-STEM operation. These reconstructions also revealed subtle oxygen and titanium displacements relative to their centrosymmetric cubic positions, consistent with the onset of a low-temperature ferroelectric phase, demonstrating how non-raster scanning can recover delicate structural signatures in dose-sensitive oxide systems.

Inward spiral datasets were also acquired; however, these reconstructions did not converge reliably.

Downloaded from academic.oup.com/mam/article/32/4/ozag080/8754136 by guest on 10 November 2026

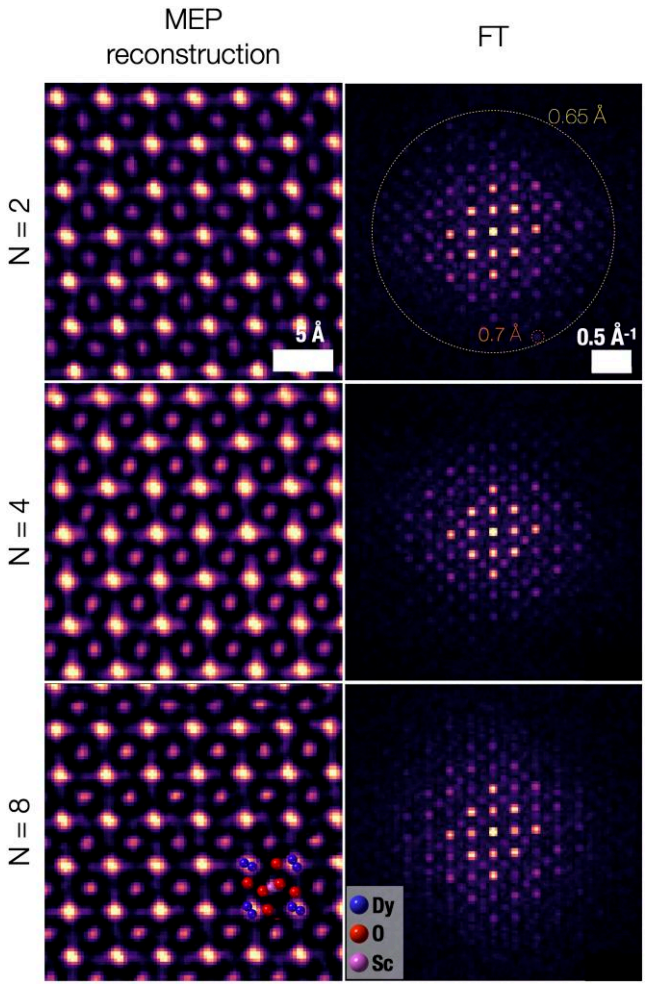


Fig. 5. Ptychographic phase reconstructions of $DyScO_3$ obtained using mixed-mode multislice algorithms (2 probe modes, 18 slices, 2 nm thickness, 20 nm defocus). Comparisons are shown for N-sequential scan patterns ($N = 2$, 4, 8). FFTs of the reconstructions include a reference circle at 0.65 Å, with visible Bragg peaks extending to ~0.7 Å. High-resolution information remains consistent despite increasing scan-sequence complexity.

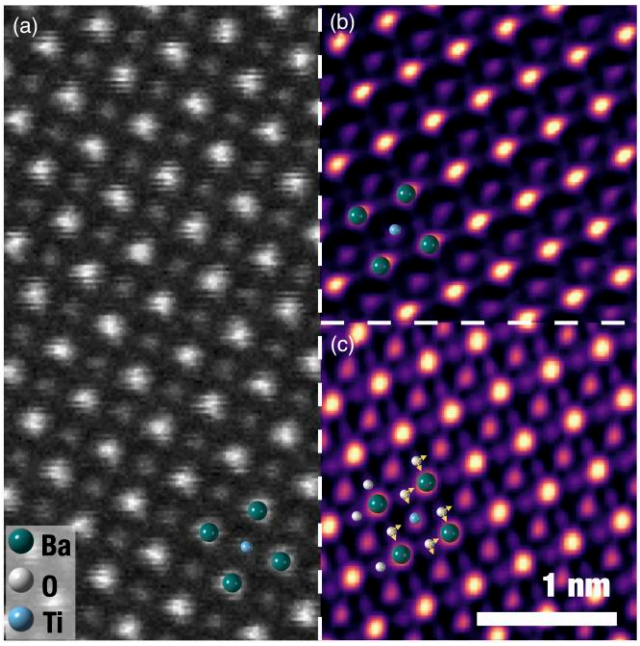


Fig. 6. Comparison of raster HAADF (**a**) and ptychographic reconstructions (**b, c**) of a free-standing BTO thin film acquired at cryogenic temperature. The HAADF image in (**a**) was acquired separately in Velox under raster scanning and is not recorded simultaneously with the ptychographic datasets; it is shown unfiltered to reflect the cryogenic acquisition conditions and associated drift and mechanical instabilities. (**b**) Ptychographic reconstruction from a raster scan. (**c**) Ptychographic reconstruction from an outward spiral scan. Oxygen columns are resolved in the spiral-scan ptychographic image, and no significant scan-induced artifacts are visible, demonstrating the suitability of programable scanning for cryogenic experiments.

Undercryogenic conditions, ptychographic convergence can be sensitive to drift, reduced signal-to-noise ratio, and mechanical instabilities, and we cannot attribute this behavior to the scan trajectory alone. We therefore present only the outward spiral reconstruction, which converged consistently and clearly resolves the oxygen columns.

Discussion

Temporal Dose Efficiency and Scan-Trajectory Effects

The electron fluence employed in this study (10^5–10^7 $e^-/Å^2$) is typical for atomic-resolution EELS mapping and ptychographic STEM reconstruction, where high signal-to-noise ratios and sub-ångström phase retrieval require relatively large total dose. Under these conditions, the scan strategy does not reduce the total electron dose, but governs how dose is distributed in space and time during acquisition. Although temporally separated probe visits may theoretically mitigate cumulative radiolytic excitation, under the fast acquisition conditions used here the dominant effect is mechanical and electronic settling of the scan system.

DSO was intentionally selected as a structurally robust reference material. No visible radiation-induced damage was observed for any trajectory, including raster scanning. Consequently, differences between scan strategies arise from scan dynamics and dose-delivery uniformity rather than beam-induced structural degradation. Demonstrating radiolysis mitigation would require substantially more beam-sensitive materials.

In *N*-sequential scan modes, where there is no line flyback delay, large pixel jumps rely solely on intrinsic scan-coil settling between successive probe positions. When the commanded displacement approaches several lattice spacings, incomplete stabilization of the deflection system can introduce systematic positional offsets that propagate into real-space distortions and reciprocal-space artifacts. Mullarkey et al. have shown that discontinuous probe motion reduces *beam efficiency* and can introduce position-dependent exposure asymmetry across an image (Mullarkey et al., 2022). Trajectories involving large probe jumps, can therefore, introduce systematic distortions. In this work, the $N = 4$ sequential scan showed the largest deviation from HAADF spacings and degraded atomic-resolution chemical maps (Fig. 3), consistent with probe-settling errors and scan-coil stabilization delays.

For raster scanning, the measured flyback time (~200 μs) contributes less than 0.3% overhead to the 128 × 128 acquisition with 677-μs dwell time. This indicates that flyback-induced distortions are minimal, confined to at most the first

Downloaded from academic.oup.com/mam/article/32/4/ozag080/8754136 by guest on 10 November 2026

few pixels, and not visible in the remainder of the image. Continuous spiral trajectories have no flyback and minimize probe-settling overhead by maintaining uninterrupted probe motion. Consistent with the results, both spiral strategies produced chemical maps with signal-to-noise ratios comparable to raster scans while avoiding discontinuity-induced artifacts. A slight reduction in signal toward the scan periphery is observed for spiral in in Figure 3, reflecting intrinsic oversampling of the central region. No beam damage was detected in this region. A localized intensity feature is observed near the center of the spiral-out scan. Its origin cannot be unambiguously determined and may arise either from pre-existing surface contamination or beam-induced accumulation during acquisition. Because spiral trajectories visit neighboring pixels in the central region closer in time, the temporal separation between adjacent probe positions is reduced, which may locally increase accumulated exposure within a small spatial neighbourhood. While no structural degradation was detected in DSO, this effect could become significant for more beam-sensitive materials.

For ptychography, similar electron-doses are typically required to obtain sub-ångström phase reconstructions (Chen et al., 2020), providing a comparable basis for evaluating scan trajectory effects. In this context, continuous probe motion can improve probe overlap uniformity and diffraction stability rather than reducing radiation damage. More generally, non-raster trajectories influence measurement outcomes through their temporal ordering, probe-motion continuity, and scan geometry. In EELS, the resulting signal quality is comparable to conventional raster scans. In ptychography, continuous motion can enhance overlap uniformity, improve reconstruction stability, and reduce scan-induced artifacts.

Scan-Induced Artifacts in ADF and EELS

Programable scan trajectories influence imaging fidelity and spectroscopic reliability through a combination of probe-dynamics, sampling geometry, and temporal dose distribution. Mechanical effects such as coil hysteresis, probe-settling delays, and flyback motion introduce position-dependent deviations between the commanded and actual probe positions during rapid scan motion (Sang et al., 2017). At the same time, the temporal ordering of pixel visits determines how dose accumulates locally within the specimen. These effects propagate differently into ADF imaging, atomic-resolution EELS mapping, and reciprocal-space representations of the data.

To further evaluate trajectory-induced distortions, FFTs were computed from the simultaneously acquired ADF frames for each scan pattern. Even in the raw FFTs, noticeable differences in spatial-frequency completeness and azimuthal symmetry were observed. After applying Hanning filtering, quartile-based thresholding, and cropping, trajectory-specific signatures became more apparent.

For the $N = 4$ sequential scan, the FFT exhibits additional peaks that do not correspond to DSO Bragg reflections. These arise from block-wise distortions introduced by the scan pattern itself. Because each 4×4 sub-raster is scanned independently, large probe jumps occur at block boundaries. The limited coil-settling time produces sharp, non-lattice distortions, such as truncated or kinked atomic columns, that are visible in the ADF image. These distortions act as a multiplicative real-space modulation with periodicity most likely related to the block size, resulting in convolution artifacts in the FFT. The additional peaks are not symmetrically arranged around the Bragg reflections and extend to frequencies beyond the true lattice information. No additional reflections consistent with the expected orthorhombic superlattice periodicity are resolved in this FFT, indicating that the observed features originate from scan-induced modulation rather than crystallography.

In contrast, the random scan shows a different artifact signature. Because the probe jumps between widely separated positions, the coil-settling error is uncorrelated in real space. This produces a diffuse, noise-like background in the FFT rather than the structured pattern seen for $N = 4$. The underlying Bragg reflections are still visible, but they appear less azimuthally uniform and decay more rapidly with spatial frequency, consistent with the noisier real-space maps and uneven dose-per-pixel distribution.

Raster and spiral trajectories demonstrate different trade-offs. Raster scanning is mechanically simple and maintains uniform temporal sampling and adjacent-pixel continuity, preserving the highest degree of atomic-column definition in EELS maps. However, the repetitive line-by-line motion, together with external factors such as mechanical vibrations and electrical interference, introduces asymmetries that accumulate along the slow-scan direction. This produces faint vertical streaks in ADF FFTs (green arrows in Fig. 3).

Spiral FFTs show sharper and more isotropic Bragg peaks with reduced streaking, consistent with smoother coil excitation and reduced directional hysteresis. However, a slight anisotropy remains at the highest spatial frequencies. Although the square spiral maintains a uniform spatial grid, the sequential scan introduces non-uniform dose delivery over time. In the central region, neighboring pixels are visited in rapid succession, whereas toward the edges the time between revisits increases as the probe covers a larger area.

Additionally, changes in scan direction at the spiral corners introduce direction-dependent probe dynamics. Combined with sample drift, this can produce weak anisotropy in both ADF and EELS images. These effects likely contribute to the mild directional variation in FFT intensity observed here, consistent with scan-direction-dependent distortions reported by Sang et al. (2017).

Both raster and spiral scans avoid block-aliasing artifacts, but differ in how probe dynamics and sampling geometry distribute residual distortions. Close inspection of the spiral EELS maps reveals a faint quadrant-like pattern that follows the scan trajectory. This arises from the continuously changing probe direction as it rotates across the field of view and represents a spatial registration artifact rather than beam-induced damage. Consistent with this interpretation, the core-loss EELS spectra (Sc L3, 2, Dy M5, 4, O K) remain essentially unchanged across scan patterns (Supplementary Fig. S4). Peak positions, edge shapes, and relative intensities are preserved, indicating that chemical composition, oxidation state, and fine-structure analysis are robust to scan trajectory under the conditions explored here.

This trade-off cannot be explained by differences in scan efficiency alone, which vary by only 0.3% between trajectories. Instead, it reflects differences in how sampling is distributed in space and time. Previous work on non-raster scan strategies has shown that deviations from uniform sampling require trajectory-dependent timing corrections to preserve spatial fidelity (Velazco et al., 2020). This highlights that image quality

Downloaded from academic.oup.com/mam/article/32/4/ozag080/8754136 by guest on 10 November 2026

depends not only on total acquisition time, but also on how measurements are ordered.

However, this same change in sampling also alters how signal is accumulated at the atomic scale. While spiral scans reduce scan-induced distortions and improve robustness to drift, they can lead to reduced peak contrast and less well-defined atomic columns in EELS maps, particularly for low-signal edges.

In this sense, improved artifact suppression and reduced spatial contrast arise from the same underlying change in probe motion. The choice of scan trajectory therefore reflects a trade-off between minimizing distortions and preserving spatial localization and contrast.

Drift Behavior Across Scan Trajectories

Drift was quantified from frame-to-frame registration over the 15-pass acquisition and is shown in Supplementary Figure S5 for raster, spirals, $N = 2$, $N = 4$, and random scans. All non-spiral patterns display a predominantly unidirectional cummulative drift of ~1–2 nm over the 15 passes. In contrast, both spiral trajectories follow a more distributed path that samples multiple in-plane directions (Supplementary Figs. S5b, S5c)), which correlates with a reduction in periodic scan artifacts. These effects are reflected in the EELS results discussed below, where the same redistribution of sampling influences both artifact suppression and spatial contrast.

This behavior is consistent with previous work showing that drift-induced distortion depends on the relative orientation between drift and scan direction (Sang et al., 2016). In raster imaging, this leads to the characteristic streaks along the slow-scan direction in the Fourier transform. After applying the standard drift-correction procedure, spiral EELS maps retain contrast comparable to the raster case, despite differences in the raw drift paths. Because the scan direction in a spiral continuously rotates, it provides additional directional information that can help improve intra-frame drift correction (Sang & LeBeau, 2014).

Standard raster-based approaches rely on line-by-line assumptions that do not apply to continuously varying trajectories, and care must be taken to account for the non-uniform sampling and changing beam direction. More general correction schemes are therefore required, such as real-space approaches (Jones & Nellist, 2013) or multi-frame registration strategies. Rigid and non-rigid registration across scans acquired at different orientations has been shown to improve drift estimation robustness (Sang & LeBeau, 2014; Ophus et al., 2016), but has not yet been systematically evaluated across different scan trajectories. Spiral's directional diversity could, however, reduce the need for multiple scan orientations for robust drift estimation, as previously explored in rectangular scan strategies (Velazco et al., 2020).

Although a full quantitative description of drift–trajectory interactions is beyond the scope of this work, the present results suggest that spiral scans provide more isotropic sampling. This reduces the strong directional bias present in raster scans and makes distortions easier to distinguish from genuine sample structure. As such, spiral trajectories can offer a practical advantage for drift-sensitive measurements when appropriate correction strategies are used. A systematic evaluation across scan trajectories remains an important direction for future work.

Ptychography Tolerates Large Pixel Jumps

Ptychographic reconstruction differs fundamentally from conventional STEM imaging in that it does not rely on a single pixel-by-pixel intensity measurement, but instead uses redundant, overlapping diffraction information to iteratively recover both the object and the probe (Dwivedi et al., 2018; Ophus, 2019; Savitzky et al., 2021; Varnavides et al., 2024). As long as probe overlap, reciprocal-space coverage, and diffraction signal-to-noise ratio remain sufficient, moderate scan-path irregularities and probe-position errors can be absorbed by the reconstruction algorithm.

This robustness is evident in the DSO datasets shown in Figure 5. Despite the severe trajectory-induced distortions observed in the corresponding ADF and EELS maps for increasing N, the ptychographic phase reconstructions for $N = 2$, 4, and 8 exhibit nearly identical lattice resolution and atomic contrast. The FFTs of the reconstructed phase images show Bragg reflections extending to ~0.7 Å for all scan patterns, with no visible scan-trajectory-related artifacts, even for pixel jumps approaching the interatomic spacing ($N = 8$).

At the acquisition conditions used here (sufficient electron fluence and probe overlap), increasing pixel jump distance does not measurably degrade structural fidelity in the ptychographic reconstruction. This contrasts strongly with the behavior observed in ADF and EELS, where non-uniform probe motion directly translates into real-space and reciprocal-space artifacts. These results demonstrate that ptychography is more tolerant to non-ideal scan trajectories than ADF and EELS.

Cryogenic Spiral Scanning in Free-Standing BTO: Resolving Oxygen Octahedral Shifts

Our analysis on DSO demonstrates that electron ptychography is intrinsically robust to moderate probe-position errors. However, reconstruction convergence and quality still depend on how probe overlap is distributed across the scan. Studies in X-ray ptychography have shown that spiral trajectories are significantly more tolerant to positioning jitter, Poisson noise, and motor-settling errors than raster scans (Huang et al., 2014), particularly under low-dose or cryogenic conditions where drift is unavoidable. A continuous spiral path removes discrete scan interruptions and produces a more uniform and aperiodic sampling of probe positions, improving overlap homogeneity across the field of view.

In our cryogenic BTO experiments, the combination of spiral sampling, defocused illumination, and mixed-state reconstruction explains why the spiral ptychographic reconstruction in Figure 6c resolves oxygen columns and subtle octahedral displacements more clearly than the raster counterpart in Figure 6b, despite identical electron fluence and reconstruction parameters. The six probe modes used for the raster and spiral datasets are shown in Supplementary Figure S6.

BTO undergoes a series of temperature-dependent structural phase transitions, including cubic, tetragonal, orthorhombic, and rhombohedral symmetries, driven by displacements of Ti atoms within the TiO_6 octahedra. This gives rise to spontaneous polarization and ferroelectric behavior. At low temperature, reductions in crystallographic symmetry are expressed through subtle atomic shifts, particularly of the oxygen sublattice, which define the octahedral tilt pattern and associated dipole moment.

Downloaded from academic.oup.com/mam/article/32/4/ozag080/8754136 by guest on 10 November 2026

Our cryogenic experiments demonstrate that programable spiral scanning provides an advantage in resolving these delicate structural changes. Ptychographic reconstructions from conventional raster scans resolved Ba and Ti columns and only faint oxygen contrast (Fig. 6b). In contrast, outward spiral scanning not only improved oxygen column visibility but also revealed a slight displacement of oxygen atoms consistent with an octahedral shift (Fig. 6c). This shift, coupled with subtle Ti displacements within the TiO_6 framework, implies the presence of a low-temperature ferroelectric phase rather than the centrosymmetric cubic phase observed at room temperature. However, the depth resolution of ptychographic reconstructions is limited, and these measurements are sensitive only to projected 2D displacements. We can therefore confirm the presence of in-plane oxygen shifts, but a full three-dimensional displacement pattern cannot be resolved within this dataset.

The detected displacement pattern is consistent with the onset of a rhombohedral-like phase, as described in recent reports (Bull et al., 2021). While 2D projections cannot fully resolve three-dimensional displacement vectors, the observed symmetry breaking and oxygen octahedral shift are compatible with this interpretation. Importantly, spiral scanning was essential for achieving the required signal-to-noise ratio and for suppressing scan-induced artifacts that would otherwise obscure these subtle features.

Looking forward, integration of multislice ptychography with programable scanning could enable full 3D mapping of octahedral tilts and cation displacements, providing a direct pathway for quantifying ferroelectric polarization at the atomic scale under cryogenic conditions. Such capability would represent a critical advance for studying other phase transitions, polarization dynamics, and strain-engineered ferroelectrics with minimal beam-induced damage.

Scan Strategy Robustness Across Modalities

Across both DSO and BTO datasets, programable scan patterns produced consistent ptychographic reconstructions without introducing structural distortions or loss of resolution. Despite significant variations in probe trajectory, the highest-order Bragg reflections remained comparable across scan strategies, including for $N = 8$. In contrast, virtual BF and ADF images from the same datasets exhibit clear scan-pattern artifacts, particularly at higher N, where large probe jumps and sparse sampling lead to banding, pixelation, and non-uniform contrast. Representative virtual BF images reconstructed from the defocused DSO datasets are shown in **Supplementary Figure S7**, where the underlying scan-pattern imprint is visible.

For EELS, the effect is more nuanced. While core-loss spectra (Dy, Sc, and O edges) remain consistent across scan patterns, FFT analysis and Atomap-based measurements show that scan trajectory influences the preservation of crystallographic information. Half-order reflections associated with orthorhombic tilts are retained for raster and partially for spiral scans, but are suppressed for larger N and random trajectories, indicating reduced positional fidelity rather than changes in chemical signal.

These results demonstrate a modality-dependent response to scan trajectory: ptychography remains robust to probe-path irregularities due to redundant diffraction sampling, whereas imaging and atomic-resolution mapping are more sensitive to probe-position errors and temporal dose variations.

Conclusion

In this work, we show that programable electron-beam scanning provides a practical route to control both the spatial and temporal distribution of dose in scanning transmission electron microscopy. By systematically comparing raster, spiral, and N-sequential trajectories across atomic-resolution EELS, ADF, and ptychographic datasets, we establish guidelines for selecting scan strategies in dose-sensitive experiments.

Our findings highlight three key insights:

1. **Ptychography tolerates scan irregularities.** Iterative phase retrieval reliably recovers high-resolution structural information even from non-uniform and discontinuous scan trajectories, enabling flexible dose redistribution without significant loss of spatial resolution.
2. **EELS and ADF remain trajectory-sensitive.** In contrast, large probe jumps, flyback delays, and non-uniform temporal dose distributions introduce positional errors that degrade atomic-column definition and crystallographic fidelity. While core-loss spectra remain consistent, scan trajectory directly impacts the spatial registration of chemical information.
3. **Spiral scanning provides a robust compromise.** Continuous probe motion suppresses flyback artifacts and reduces coil-settling errors while maintaining spatial fidelity comparable to raster scanning. Although spiral trajectories redistribute dose radially, no degradation in structural or spectroscopic quality was observed under the conditions used here.

Overall, these results demonstrate that scan trajectory is a critical but tunable parameter in STEM. Programable scanning enables dose redistribution strategies that can be exploited in ptychography with minimal penalty, but quantitative atomic-resolution EELS and ADF imaging require careful control of probe position and temporal dose uniformity. These findings provide a framework for selecting scan strategies according to the spatial-fidelity requirements of the measurement, and establish programable scanning as a versatile tool for advanced 4D-STEM and spectroscopic imaging.

Availability of Data and Materials

Scan trajectory implementation using custom DigitalMicrograph scripting and Python code are available at Zenodo, DOI: 10.5281/zenodo.18834914.

Supplementary Material

To view supplementary material for this article, please visit https://doi.org/10.1093/mam/ozag080.

Acknowledgments

This work was made possible by the EPSRC Cryo-Enabled Multi-microscopy for Nanoscale Analysis in the Engineering and Physical Sciences EP/V007661/1. M.P., Y.L. and M.S.C. acknowledge funding from the Royal Society Tata University Research Fellowship (URF\R1\201318) and Royal Society Enhancement Award RF\ERE\210200EM1. G.T. EPSRC Centre for Doctoral Training in the Advanced Characterisation of Materials (CDTACM)(EP/S023259/1) for funding their Ph.D. studentships and G.T. acknowledges

Downloaded from academic.oup.com/mam/article/32/4/ozag080/8754136 by guest on 10 November 2026

Cameca Ltd. for co-funding their PhD. Work at the Molecular Foundry was supported by the Office of Science, Office of Basic Energy Sciences, of the U.S. Department of Energy under Contract No. DE-AC02-05CH11231. A preprint version of this manuscript was published in arXiv (arXiv:2509.10726) (Palos et al., 2025).

Author Contributions Statement

M.S.C. and M.P. collected the experimental data. M.P., L.S., and M.S.C. processed the EELS data. M.P. processed the ptychography data using py4DSTEM with input from S.R., C.O. and M.S.C. All authors contributed to the project planning and writing.

Financial Support

None.

Conflict of Interest

L.S. is affiliated with Gatan Inc., the manufacturer of electron microscopy instrumentation used in this study. The remaining authors declare no competing interests.

References

Barzilay M & Ivry Y (2020). Formation and manipulation of domain walls with 2 nm domain periodicity in batio 3 without contact electrodes. *Nanoscale* **12**(20), 11136–11142. https://doi.org/10.1039/d0nr01747g

Béché A, Goris B, Freitag B & Verbeeck J (2016). Development of a fast electromagnetic beam blanker for compressed sensing in scanning transmission electron microscopy. *Appl Phys Lett* **108**(9). https://doi.org/10.1063/1.4943086

Bull CL, Ridley CJ, Knight KS, Funnell NP & Gibbs AS (2021). Comprehensive determination of the high-pressure structural behaviour of batio3. *Mater Adv* **2**, 6094–6103. https://doi.org/10.1039/D1MA00651G

Chen Z, Odstrcil M, Jiang Y, Han Y, Chiu M-H, Li L-J & Muller DA (2020). Mixed-state electron ptychography enables sub-angstrom resolution imaging with picometer precision at low dose. *Nat Commun* **11**(1). https://doi.org/10.1038/s41467-020-16688-6

Chezganov DS, Vlasov EO, Pashnina EA, Chuvakova MA, Esin AA, Greshnyakov ED & Shur VY (2019). Domain structure formation by electron beam irradiation in lithium niobate crystals at elevated temperatures. *Appl Phys Lett* **115**(9). https://doi.org/10.1063/1.5108962

Conroy M, Moore K, O'Connell E, Jones L, Downing C, Whamore R, Gruverman A, Gregg M & Bangert U (2020). Probing the dynamics of topologically protected charged ferroelectric domain walls with the electron beam at the atomic scale. *Microsc Microanal* **26**(S2), 3030–3032. https://doi.org/10.1017/S1431927620023594

Dwivedi P, Konijnenberg AP, Pereira SF & Urbach HP (2018). Lateral position correction in ptychography using the gradient of intensity patterns. *Ultramicroscopy* **192**, 29–36. https://doi.org/10.1016/j.ultramic.2018.04.004

Dyck O, Ziatdinov M, Lingerfelt DB, Unocic RR, Hudak BM, Lupini AR, Jesse S & Kalinin SV (2019). Atom-by-atom fabrication with electron beams. *Nat Rev Mater* **4**(7), 497–507. https://doi.org/10.1038/s41578-019-0118-z

Ede JM & Beanland R (2020). Partial scanning transmission electron microscopy with deep learning. *Sci Rep* **10**(1). https://doi.org/10.1038/s41598-020-65261-0

Egerton RF (2003). New techniques in electron energy-loss spectroscopy and energy-filtered imaging. *Micron* **34**(3–5), 127–139. https://doi.org/10.1016/s0968-4328(03)00023-4

Egoavil R, Gauquelin N, Martinez GT, Van Aert S, Van Tendeloo G & Verbeeck J (2014). Atomic resolution mapping of phonon excitations in stem-eels experiments. *Ultramicroscopy* **147**, 1–7. https://doi.org/10.1016/j.ultramic.2014.04.011

Goodge BH, Bianco E, Schnitzer N, Zandbergen HW & Kourkoutis LF (2021). Atomic-resolution cryo-stem across continuously variable temperatures. *Microsc Microanal* **26**(3), 439–446. https://doi.org/10.1017/S1431927620001427

Hart JL, Liu S, Lang AC, Hubert A, Zukauskas A, Canalias C, Beanland R, Rappe AM, Arredondo M & Taheri ML (2016). Electron-beam-induced ferroelectric domain behavior in the transmission electron microscope: Toward deterministic domain patterning. *Phys Rev B* **94**(17), 174104. https://doi.org/10.1103/PhysRevB.94.174104

Huang X, Yan H, Harder R, Hwu Y, Robinson IK & Chu YS (2014). Optimization of overlap uniformness for ptychography. *Opt Express* **22**(10), 12634–12644. https://doi.org/10.1364/OE.22.012634

Jannis D, Hofer C, Gao C, Xie X, Béché A, Pennycook TJ & Verbeeck J (2022*a*). Event driven 4D stem acquisition with a timepix3 detector: Microsecond dwell time and faster scans for high precision and low dose applications. *Ultramicroscopy* **233**, 113423. https://doi.org/10.1016/j.ultramic.2021.113423

Jannis D, Velazco A, Béché A & Verbeeck J (2022*b*). Reducing electron beam damage through alternative stem scanning strategies, part ii: Attempt towards an empirical model describing the damage process. *Ultramicroscopy* **240**, 113568. https://doi.org/10.1016/j.ultramic.2022.113568

Jones L & Nellist PD (2013). Identifying and correcting scan noise and drift in the scanning transmission electron microscope. *Microsc Microanal* **19**(4), 1050–1060. https://doi.org/10.1017/s1431927613001402

Lin J, Cretu O, Zhou W, Suenaga K, Prasai D, Bolotin KI, Cuong NT, Otani M, Okada S, Lupini AR, Idrobo J-C, Caudel D, Burger A, Ghimire NJ, Yan J, Mandrus DG, Pennycook SJ & Pantelides ST (2014). Flexible metallic nanowires with self-adaptive contacts to semiconducting transition-metal dichalcogenide monolayers. *Nat Nanotechnol* **9**(6), 436–442. https://doi.org/10.1038/nnano.2014.81

Mille N, Yuan H, Vijayakumar J, Stanescu S, Swaraj S, Desjardins K, Favre-Nicolin V, Belkhou R & Hitchcock AP (2022). Ptychography at the carbon k-edge. *Commun Mater* **3**(1). https://doi.org/10.1038/s43246-022-00232-8

Mullarkey T, Peters JJP, Downing C & Jones L (2022). Using your beam efficiently: Reducing electron dose in the stem via flyback compensation. *Microsc Microanal* **28**(4), 1428–1436. https://doi.org/10.1017/S1431927621013908

Mundet B, Hadjimichael M, Fowlie J, Korosec L, Varbaro L, Domínguez C, Triscone J-M & Alexander DT (2024). Mapping orthorhombic domains with geometrical phase analysis in rare-earth nickelate heterostructures. *APL Mater* **12**(3). https://doi.org/10.1063/5.0180998

Nicholls D, Lee J, Amari H, Stevens AJ, Mehdi BL & Browning ND (2020). Minimising damage in high resolution scanning transmission electron microscope images of nanoscale structures and processes. *Nanoscale* **12**, 21248–21254. https://doi.org/10.1039/D0NR04589F

Nord M, Vullum PE, MacLaren I, Tybell T & Holmestad R (2017). Atomap: A new software tool for the automated analysis of atomic resolution images using two-dimensional gaussian fitting. *Adv Struct Chem Imaging* **3**(1) article number 9. https://doi.org/10.1186/s40679-017-0042-5

Ophus C (2019). Four-dimensional scanning transmission electron microscopy (4d-stem): From scanning nanodiffraction to ptychography and beyond. *Microsc Microanal* **25**(3), 563–582. https://doi.org/10.1017/S1431927619000497

Ophus C (2023). Quantitative scanning transmission electron microscopy for materials science: Imaging, diffraction, spectroscopy, and

Downloaded from academic.oup.com/mam/article/32/4/ozag080/8754136 by guest on 10 November 2026

tomography. *Annu Rev Mater Res* **53**(1), 105–141. https://doi.org/10.1146/annurev-matsci-080921-092646

Ophus C, Ciston J & Nelson CT (2016). Correcting nonlinear drift distortion of scanning probe and scanning transmission electron microscopies from image pairs with orthogonal scan directions. *Ultramicroscopy* **162**, 1–9. https://doi.org/10.1016/j.ultramic.2015.12.002

Ortega E, Nicholls D, Browning ND & de Jonge N (2021). High temporal-resolution scanning transmission electron microscopy using sparse-serpentine scan pathways. *Sci Rep* **11**, 24301. https://doi.org/10.1038/s41598-021-03557-4

Palos M, Spillane L, Topore G, Li Y, Pesquera D, Ophus C, Ribet SM & Conroy MS (2025). 'Programmable beam control for electron energy-loss spectroscopy and ptychography.' arXiv, arXiv:2509.10726v1, preprint.

Pei X, Zhou L, Huang C, Boyce M, Kim JS, Liberti E, Hu Y, Sasaki T, Nellist PD, Zhang P, Stuart DI, Kirkland AI & Wang P (2023). Cryogenic electron ptychographic single particle analysis with wide bandwidth information transfer. *Nat Commun* **14**(1), 2781. https://doi.org/10.1038/s41467-023-38268-0

Peters JJ, Reed BW, Jimbo Y, Noguchi K, Müller KH, Porter A, Masiel DJ & Jones L (2024). Event-responsive scanning transmission electron microscopy. *Science* **385**(6708), 549–553. https://doi.org/10.1126/science.ado8579

Roede ED, Mosberg AB, Evans DM, Bourret E, Yan Z, van Helvoort ATJ & Meier D (2021). Contact-free reversible switching of improper ferroelectric domains by electron and ion irradiation. *APL Mater* **9**(2). https://doi.org/10.1063/5.0038909

Sang X & LeBeau JM (2014). Revolving scanning transmission electron microscopy: Correcting sample drift distortion without prior knowledge. *Ultramicroscopy* **138**, 28–35. https://doi.org/10.1016/j.ultramic.2013.12.004

Sang X, Lupini AR, Ding J, Kalinin SV, Jesse S & Unocic RR (2017). Precision controlled atomic resolution scanning transmission electron microscopy using spiral scan pathways. *Sci Rep* **7**(1). https://doi.org/10.1038/srep43585

Sang X, Lupini AR, Unocic RR, Chi M, Borisevich AY, Kalinin SV, Endeve E, Archibald RK & Jesse S (2016). Dynamic scan control in stem: Spiral scans. *Adv Struct Chem Imaging* **2**(1). https://doi.org/10.1186/s40679-016-0020-3

Savitzky BH, Baggari IE, Clement CB, Waite E, Goodge BH, Baek DJ, Sheckelton JP, Pasco C, Nair H, Schreiber NJ, Hoffman J, Admasu AS, Kim J, Cheong S-W, Bhattacharya A, Schlom DG, McQueen TM, Hovden R & Kourkoutis LF (2018). Image registration of low signal-to-noise cryo-stem data. *Ultramicroscopy* **191**, 56–65. https://doi.org/10.1016/j.ultramic.2017.06.007

Savitzky BH, Zeltmann SE, Hughes LA, Brown HG, Zhao S, Pelz PM, Pekin TC, Barnard ES, Donohue J, DaCosta LR, Kennedy E, Xie Y, Janish MT, Schneider MM, Herring P, Gopal C, Anapolsky A, Dhall R, Bustillo KC, Ercius P, Scott MC, Ciston J, Minor AM & Ophus C (2021). py4dstem: A software package for four-dimensional scanning transmission electron microscopy data analysis. *Microsc Microanal* **27**(4), 712–743. https://doi.org/10.1017/S1431927621000477

Susi T, Meyer JC & Kotakoski J (2017). Manipulating low-dimensional materials down to the level of single atoms with electron irradiation. *Nat Rev Mater*, 163–172. https://doi.org/10.1016/j.ultramic.2017.03.005

Torruella P, Halimi A, Tovaglieri L, Lichtensteiger C, Alexander DTL & Hébert C (2025). A multiscale Bayesian approach to quantification and denoising of energy-dispersive x-ray data. *Mach Learn Sci Technol* **6**(2), 025043. https://doi.org/10.1088/2632-2153/add8e1

Turner R, Nord M, Velazco A & Verbeeck J (2020). Optimal scanning strategies for high-fidelity stem imaging. *Ultramicroscopy* **218**, 113085. https://doi.org/10.1016/j.ultramic.2020.113085

Varnavides G, Ribet SM, Zeltmann SE, Yu Y, Savitzky BH, Byrne DO, Allen FI, Dravid VP, Scott MC & Ophus C (2024). 'Iterative phase retrieval algorithms for scanning transmission electron microscopy.' arXiv, arXiv:2309.05250v2, preprint.

Velazco A, Béché A, Jannis D & Verbeeck J (2022). Reducing electron beam damage through alternative stem scanning strategies, part i: Experimental findings. *Ultramicroscopy* **232**, 113398. https://doi.org/10.1016/j.ultramic.2021.113398

Velazco A, Nord M, Béché A & Verbeeck J (2020). Evaluation of different rectangular scan strategies for stem imaging. *Ultramicroscopy* **215**, 113021. https://doi.org/10.1016/j.ultramic.2020.113021

Verbeeck J & Van Aert S (2004). Model based quantification of eels spectra. *Ultramicroscopy* **101**(2), 207–224. https://doi.org/10.1016/j.ultramic.2004.06.004

Volk TR, Kokhanchik LS, Bodnarchuk YV, Gainutdinov RV, Yakimov EB & Ivleva LI (2020). Electron-beam domain patterning in sr0.61ba0.39nb2o6 crystals. *Coatings* **10**(3), 299. https://doi.org/10.3390/coatings10030299

Zobelli A, Woo SY, Tararan A, Tizei LHG, Brun N, Li X, Stéphan O, Kociak M & Tencé M (2020). Spatial and spectral dynamics in stem hyperspectral imaging using random scan patterns. *Ultramicroscopy* **212**, 112912. https://doi.org/10.1016/j.ultramic.2019.112912

Downloaded from academic.oup.com/mam/article/32/4/ozag080/8754136 by guest on 10 November 2026